

Fast detection of the main anatomical structures in digital retinal images based on intra- and inter-structure relational knowledge

José M. Molina-Casado^a, Enrique J. Carmona^{a,*}, Julián García-Feijó^{b,c,d}

^aDept of Artificial Intelligence, ETS Ingeniería Informática, Universidad Nacional de Educación a Distancia (UNED). C/ Juan del Rosal 16, 28040 Madrid, Spain

^bDept of Ophthalmology, Faculty of Medicine, Complutense University, Madrid, Spain.

^cOcular Pathology National Net OFTARED of the Institute of Health Carlos III.

^dDept of Ophthalmology, Sanitary Research Institute of the San Carlos Clinical Hospital, Madrid, Spain.

Abstract

Background and Objective: The anatomical structure detection in retinal images is an open problem. However, most of the works in the related literature are oriented to the detection of each structure individually or assume the previous detection of a structure which is used as a reference. The objective of this paper is to obtain simultaneous detection of the main retinal structures (optic disc, macula, network of vessels and vascular bundle) in a fast and robust way.

Methods: We propose a new methodology oriented to accomplish the mentioned objective. It consists of two stages. In an initial stage, a set of operators is applied to the retinal image. Each operator uses intra-structure relational knowledge in order to produce a set of candidate blobs that belongs to the desired structure. In a second stage, a set of tuples is created, each of which contains a different combination of the candidate blobs. Next, filtering operators, using inter-structure relational knowledge, are used in order to find the winner tuple. A method using template matching and mathematical morphology is implemented following the proposed methodology.

Results: A success is achieved if the distance between the automatically detected blob center and the actual structure center is less than or equal to one optic disc radius. The success rates obtained in the different public databases were: MESSIDOR (99.33%, 98.58%, 97.92%), DIARETDB1 (96.63%, 100%, 97.75%), DRIONS (100%, n/a, 100%) and ONHSD (100%, 98.85%, 97.70%) for optic disc, macula and vascular bundle, respectively. Finally, the overall success rate obtained in this study for each structure was 99.26%, 98.69% and 98.95%, respectively. The average time of processing per image was 4.16 ± 0.72 s.

*Corresponding author. Tel.: +34 91 398 7301

Email addresses: molina.jm@iescyedra.es (José M. Molina-Casado), ecarmona@dia.uned.es (Enrique J. Carmona), jgarciafeijoo@hotmail.es (Julián García-Feijó)

Conclusions: The main advantage of the use of inter-structure relational knowledge was the reduction of the number of false positives in the detection process. The implemented method is able to simultaneously detect four structures. It is fast, robust and its detection results are competitive in relation to other methods of the recent literature.

Keywords: Retinal image, Anatomical structure detection, Optic disc, Macula, Vessel network, Vascular bundle

1. Introduction

During the eye fundus exam or retinal image analysis, ophthalmologists look for specific anatomical patterns to identify possible disease marks and establish possible diagnoses from them. Therefore, it is necessary to address the detection and segmentation of the more relevant anatomical structures (see Fig. 1) in order to automate the task of image-based diagnosis of the retina [1]. In the context of retinal image processing, the anatomical structure detection task, also called *localization* task, is normally defined as the search the one point that represents the center of the area encompassed by the structure. On the other hand, the segmentation task implies the search of the all the points that form the area or perimeter of the structure. Although both tasks are important separately, a high success rate in the detection process will greatly facilitate the success of the segmentation task. The following stages involved in the construction of an image-based diagnostic aid system will also be favored by such successes. In this work, we only focus on the detection task.

There are many arguments in the literature that justify the importance of the retinal structure detection. Thus, the detection results of the different anatomical structures can be used as reference points (landmarks) for other automated diagnosis systems in order to detect signs of several retinal diseases [2, 3, 4, 5, 6, 7]. For example, the detection of the optic disc is a prerequisite for the computation of some important diagnostic indexes for hypertensive/sclerotic retinopathy based on vasculature [6, 8]. In the same way, the proximity of a bright/dark lesion to macula indicates a higher likelihood of impaired vision and hence calls for immediate medical attention [7]. On the other hand, in order to successfully find abnormal structures in a retinal image it is often necessary to mask out the normal anatomy from the analysis [9]. For example, since the OD may be easily confounded with large exudative lesions by image analysis techniques, its detection is also important to exclude it from the set of possible lesions [6]. A similar argument applies to fovea when the objective is to automatically detect retinal hemorrhages [10]. Additionally, detecting a retinal structure is a fundamental step to segment such structure, which is not only reducing the computing time, but improving the accuracy and specificity [11]. For example, there are many approaches where the optic disc detection is used as a previous step to segment it [12, 13, 14, 15, 16]. Finally, the detection can also be used to automatically classify left and right eyes in retinal images [2].

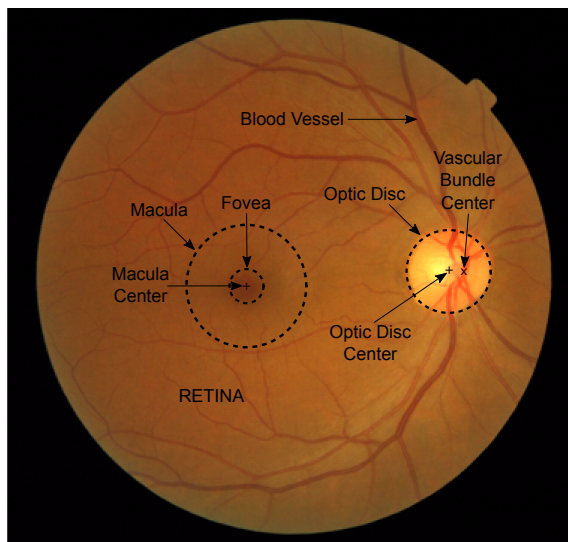


Figure 1: Main anatomical structures to consider in a retinal image (right eye).

Many strategies have been used in order to detect the different anatomical structures in retinal images. In a first classification, the different approaches can be divided into two main groups: those that only use the properties of each structure in order to detect it separately and those that, additionally, also use the relational knowledge between different structures to facilitate jointly the detection of two or more structures. Henceforth, the first type of knowledge will be denoted as *intra-structure relational knowledge* (intra-SRK) and the second as *inter-structure relational knowledge* (inter-SRK).

Initially, the first works addressed isolated detection of each structure, using only intra-SRK. Thus, for example, in [17], the optic disc was located by identifying the area with the highest variation in intensity of adjacent pixels; the blood vessels were identified by means of a multilayer perceptron; and the macula was identified using matching correlation with a template to locate candidate regions. This type of strategy, based on the unique use of intra-SRK, has continued to be exploited in more recent research works. However, the objective of these strategies was twofold, detecting and segmenting a specific structure. Several works on optic disc identification have gone in that direction [3, 13, 14, 15, 18]. Under this paradigm, the macula has received less attention, probably due to the fact that isolated macula detection is more difficult to solve than optic disc detection.

Other strategies have evolved into a joint use of the two types of knowledge (intra- and inter-SRK). For example, optic disc detection has been accomplished by preliminary detection of the main retinal vessel [6, 16, 19]. The main blood vessels have been identified using a modified active shape model and then the

parabolic shape has been used as a reference in order to locate the macula [20]. The optic disc detection has been exploited to constrain a candidate region where the fovea is detected [7, 21, 22]. Simultaneous detection of OD and fovea has been also addressed [23].

Following the trend of the aforementioned approaches, there also exist research works where the use of intra- and inter-SRK has been proposed in order to jointly find three different retinal structures. In [24], accurate segmentation of the vasculature and its spatial features are used to detect the optic disc and then this and a geometric model of the vasculature are used to detect the horizontal raphe and finally detect the macula. In [25], the elliptical form of the major retinal blood vessels is used to obtain approximate locations for the optic disc and macula, which are refined based on the circular edge of the former and local darkening at the latter. In [26], a k-NN regressor is utilized to predict the distance to the structures of interest using segmentation of the retinal vasculature. The point with the lowest predicted distance to the optic disc is selected as the optic disc solution and the search area for the macula is defined based on the location of the optic disc. In [27], the location of the optic disc is identified using template matching and, in order to reduce false positives due to bright areas of pathology, the vessel characteristics are also exploited. The location of the fovea is estimated as the point of lowest matched filter response within a search area determined by the optic disc location. In [4], optic disc detection and blood vessel segmentation are used to detect the macula, using the above mentioned distance relation between the macula and optic disc centers. Finally, in [5], the likelihood values for pixels to be optic disc or macula centers are computed by what is known as the *fast radial symmetry transform*, making use of vessel density estimation.

All the references mentioned above are only a representative sample of the substantial amount of approaches reported in the literature. This indicates that anatomical structure detection in retinal images is an open problem, directing efforts towards obtaining increasingly fast and robust methods. In any case, the current trend seems to be directed towards the use of the two kinds of knowledge (intra- and inter-SRK). In this work, we provide a detection methodology that follows that trend. Basically, this methodology consists of two stages. In an initial stage, a set of operators is applied to the retina image. Each operator is defined for searching a specific structure by using intra-SRK and produces a set of candidate blobs belonging to such structure. Then, in a second stage, a new set of relational operators use inter-SRK in order to filter and evaluate the set of tuples resulting from combining the different types of blobs obtained in the first stage. Finally, the winner tuple selected will contain the solution structures.

The main contribution of this work is twofold. First, a new generic methodology for the simultaneous detection of N different retinal structures is presented. It is based on the joint use of intra- and inter-SRK and is independent of the resolution and angle of field-of-view (FOV) of the original image. It exploits the three RGB channel information, avoiding the loss of information due to channel saturation problems of other approaches where a unique channel is used. In

addition, the methodology does not make assumptions about the way in which the retinal images have been acquired (i.e. fovea centered or optic disc centered) and is easily reconfigurable in sets of images where the optic disc or the macula was not visible. Second, a method based on such a methodology is instantiated for the detection of four retinal structures: optic disc, macula, main vessels and vascular bundle. This latter structure is not normally used in the literature. However, as will be seen here, the vascular bundle has allowed us to improve the robustness of the detection process by helping to eliminate false positive candidate blobs.

The rest of the paper is organized as follows. Section 2 describes the databases used in the experiments. Section 3 provides a detailed explanation of the proposed methodology and describes the method used to instantiate it. Section 4 presents the experimental results and these are discussed in Section 5. Finally, conclusions and future work are provided in Section 6.

2. Materials

We have used four different databases for the experiments: MESSIDOR [28, 29], DRIONS-DB [13, 30], ONHSD [12, 31], and DIARETDB1 [32, 33]. The MESSIDOR database contains 1200 retinal images, RGB format, 8 bits/pixel, $FOV = 45^\circ$ and three different sizes: 1440×960 , 2240×1488 and 2304×1536 . The optic disc ground truth for this database is available on the MESSIDOR web [28]. The annotations¹ of fovea centers from 1136 MESSIDOR images were created and published by the University of Huelva. The remaining 64 annotations, up to 1200, were kindly provided by the authors of [4]. The DRIONS database consists of 110 retinal images, RGB format, 8 bits/pixel, $FOV = 40^\circ$ and a size of 600×400 . Only the optic disc ground truth is provided on the web of this database [30]. Specifically, each OD center used as a reference was obtained as a result of averaging the geometric centers of two OD contours traced by two different experts. The ONHSD database contains 99 retinal images, RGB format, 8 bits/pixel, $FOV = 45^\circ$ and size of 640×480 . Here, only the optic disc ground truth is provided on the web of this database [31]. Specifically, each OD center used as a reference was obtained as a result of averaging the geometric centers of four OD contours traced by four different experts and, on the other hand, the fovea centers were annotated by our specialist in ophthalmology. Finally, the DIARETDB1 database contains 89 retinal images, RGB format, $FOV = 50^\circ$ and size of 1500×1152 . On the web of this database [32], there is no ground truth for the fovea and optic disc. Here, the OD centers were annotated by our specialist in ophthalmology and the fovea annotations were obtained from [34]. All the mentioned databases contain healthy eyes and eyes with several kinds of retinopathies. A more detailed description for each database can be consulted in their respective references.

¹http://www.uhu.es/retinopathy/muestras/Provided_Information.zip

3. Methodology and Method

The objective of the methodology here presented is to obtain joint detection of the main anatomical structures in digital retinal images: optic disc, macula, network of main vessels, and vascular bundle (see Fig. 1). The basic idea is to use both intra-SRK and inter-SRK. Figure 2 shows the scheme followed. First, the original image is normalized and then its size is reduced. Next, for each type of anatomical structure, an operator, which only uses intra-SRK, is applied in order to obtain a set of candidate blobs, each of which is a potential solution of the type of structure searched. We use the term *set of candidates* because each set should contain zero, one or more false positives and the true positive. The false positives would be associated to the existence of distractors in the image, that is, patterns which are similar to the structure to be detected. On the other hand, the true positive will correspond to the solution structure. After that, a set of tuples is created where each tuple contains a different combination of the candidate blobs. Then new operators, which use inter-SRK, are applied. One of these operators is capable of detecting false positive blobs in order to eliminate all those tuples containing them. Finally, an ultimate inter-SRK operator discards the rest of false positive tuples and selects the best tuple, where each component contains the solution blob of the respective anatomical structure.

3.1. Normalizing and resizing the original retinal image

The two objectives of this stage are to normalize the intensity and reduce the size of the input image. Intensity normalization is implemented as a contrast stretching method, that is, it is applied in order to each RGB channel covers the intensity maximum range $[0, 255]$. The reduction of size is made using a scale factor oriented to obtain a fixed image resolution value. This reduction process has several advantages. First, it helps to decrease the image processing time and it also eliminates some noisy artifacts that are present in the original image. Second, the use of a fixed resolution allows us to implement and configure a detection method that only works with that resolution and, therefore, is independent of the original size and resolution of the input image. Thus, assuming that the method will work with a standard resolution, K_0 , defined by the user, and expressed in *pixel/mm*, it is straightforward to establish the following expression:

$$K_0 = \alpha \left[\frac{A_{px}}{A_{mm^2}^\theta} \right]^{1/2} \quad (1)$$

where $A_{mm^2}^\theta$ and A_{px} represent the input image retinal area, expressed in mm^2 and pixels, respectively, and α is the scale factor needed to transform the input image to the standard resolution chosen (K_0). $A_{mm^2}^\theta$ depends on the field-of-view (FOV) of the input image, which is defined by the so-called *external angle view of the fundus camera*. Table 1 shows different values of $A_{mm^2}^\theta$ for typical values FOV [35]. A_{px} is easily calculated from the input image, counting the number of actual retinal pixels. Finally, from eq. (1), it is easy to obtain

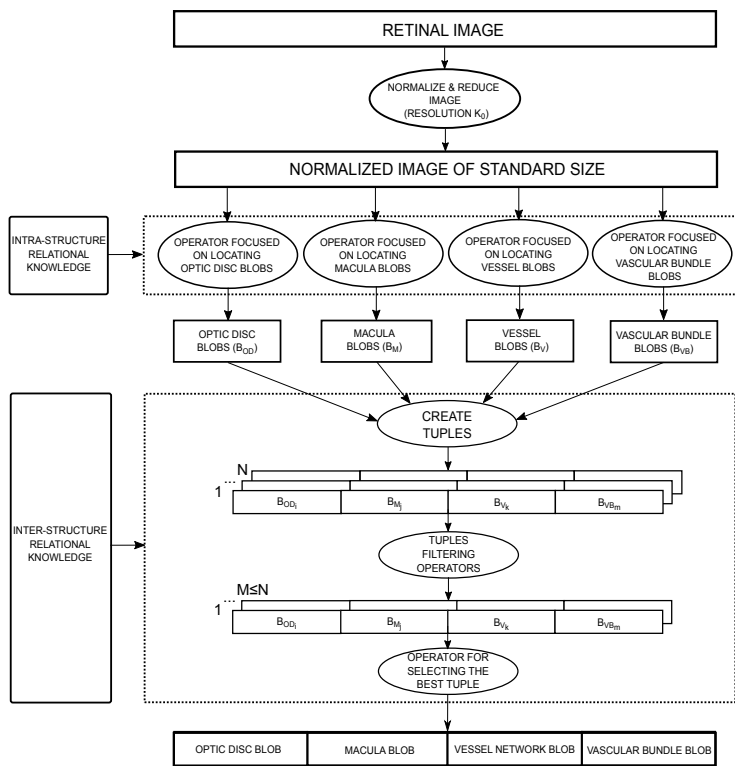


Figure 2: Block diagram of the methodology used.

the value of α , with K_0 , $A_{mm^2}^\theta$ and A_{px} known. For example, assuming that a retinal image was taken with a camera whose FOV is 40° , then, from table 1, $A_{mm^2}^\theta = 99.2 \text{ mm}^2$. If the measured diameter of the circle encompassed by the actual retinal zone is 400 pixels, then $A_{px} = \pi(400/2)^2 = 125,663.7 \text{ px}^2$. Finally, if our detection method is configured for, say, $K_0 = 10 \text{ px/mm}$, then, using eq. (1), it is immediate to obtain that the scale factor needed to reduce the size of the original image is $\alpha = 0.281$.

Table 1: Retinal area for different angle values of the field-of-view (FOV), according to [35].

FOV	Retinal Area (mm^2)
30°	56.4
40°	99.2
45°	124.8
50°	153.1

3.2. Using intra-structure relational knowledge

The intra-structure relational knowledge (intra-SRK) makes reference to all information that allows us to define a specific anatomical structure such as, for example, its shape, color, texture or contour. Here, the idea is to use different intra-SRK operators, one for each structure to detect. The final result of this stage is a set of candidate blobs for each structure. Regarding how to implement the different operators, we opted for two techniques that are well known in the field of artificial vision: *template matching* and *morphological image processing*. However, the methodology presented here is independent of the two mentioned techniques, that is, any other approach oriented to obtain a set of blob candidates for each structure could be used. The rest of this subsection describes how these intra-SRK operators are implemented for detecting each structure.

3.2.1. Optic disc blob detection

In a retinal image, the optic disc (OD) has a bright oval shape and contains the output point of the major blood vessels that supply the retina (see Fig. 1). It also contains a rounded area located approximately in its center, called the *optic cup*, which represents the brightest area of the retina in the absence of distractors.

The detection of the set of candidate OD blobs is done using correlation with template matching (TM). It is applied to each channel of the normalized and reduced input image. For each channel, the result is an image of gray levels with the property of having high values in those areas that are similar to the template. Finally, the n_{od} brightest blobs per channel in the TM output are obtained, making a total of $N_{od} = 3 \times n_{od}$ candidate optic disc blobs, where n_{od} is chosen by the user. In the blob selection process, the property that a blob is an isolated continuous region was taken into account. We start by choosing a threshold equal to the intensity of the brightest pixel of the TM output. That

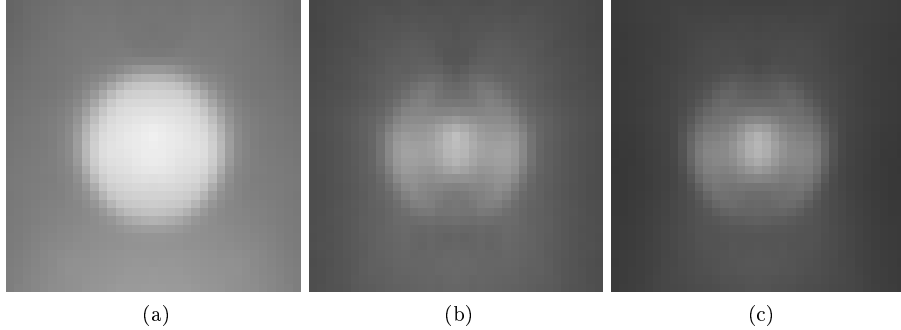


Figure 3: Optic disc templates used for each RGB channel: (a) red, (b) green, (c) blue.

pixel is called the *current blob*. Next, we progressively decrease that threshold and, in each decrement, we check if the new pixels with intensity greater than or equal to the current threshold are contiguous or not to the current blob. In the first case, the new pixels are incorporated to the current blob and the iteration continues. In the second case, the current blob is saved as a *candidate blob*, the current blob is associated to the new isolated area and the iteration continues. This process is repeated until n_{od} candidate blobs are obtained or the threshold decreases below the mean value of the TM image gray level.

The three templates were chosen with square shape and width $W_{OD} = 4 \times R_{OD}$, where R_{OD} is the mean radius of the optic disc, in pixels, at standard resolution (K_0). Knowing that the mean radius of the optic disc, expressed in *mm*, is $R_{OD,mm} = 0.925 \text{ mm}$ [8], it is easy to calculate R_{OD} , for a K_0 known, by using the following expression:

$$R_{OD} = K_0 \cdot R_{OD,mm} \quad (2)$$

The template matrix of each channel was calculated as the intensity average of different square sub-windows, with width W_{OD} , extracted from the MESSIDOR database images, at resolution K_0 , and centered on the actual geometric center of the optic disc. Specifically, 100 non-pathological images of the right eye were extracted randomly from the MESSIDOR. That number was selected experimentally (other values greater than 100 were tested but there were no improvements in the detection process). In addition, 100 new images of the left eye were generated by horizontally mirroring the 100 previous images. Thus, the template computation was done from a total of 200 images. The three RGB optic disc templates used are shown in Fig. 3.

3.2.2. Macula blob detection

In a retinal image, the macula has an oval shape and is located in the temporal area of the optic disc and delimited by the superior and inferior temporal

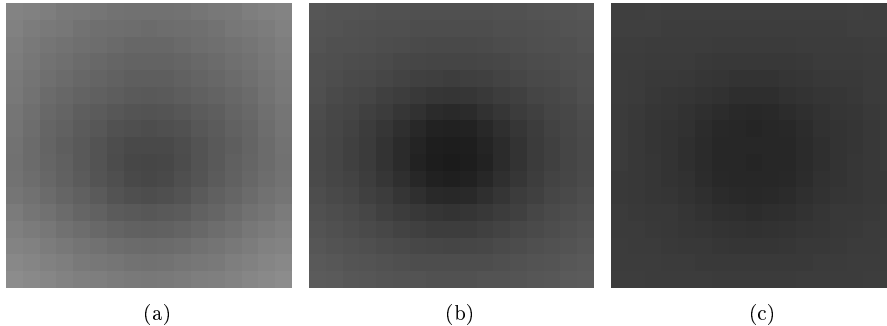


Figure 4: Macula templates used for each RGB channel: (a) red, (b) green, (c) blue.

vascular arcades (see Fig. 1). It represents the darkest area of the retina in the absence of distractors. The center of the macula is called the fovea, and it is responsible for sharp central vision.

Template matching (TM) with correlation is used to detect the set of candidate macula blobs. As with the optic disc, the n_m brightest blobs per RGB channel in the TM output are chosen, making a total of $N_m = 3 \times n_m$ candidate macula blobs, where n_m is chosen by the user. In this case, because the area covered by the macula is smaller than the optic disc area, the width of the template was $W_M = 2R_{OD}$, where R_{OD} is obtained from eq. (2). The template matrix of each channel was calculated as the intensity average of different square sub-windows, with width W_M , extracted from images belonging to the MESSIDOR database, at resolution K_0 , and centered on the actual fovea. The same 200 images as those used for computing the optic disc templates were used here. The three RGB templates used are shown in Fig. 4.

3.2.3. Retinal vessel blob detection

In a retinal image, the network of blood vessels has a tree-shaped geometry (see Fig. 1). This network can be divided into two parts: superior and inferior arcade. Both of them converge in a point which is located close to the center of the optic disc. There are morphological differences between the main and secondary vessels. The former are wider and straighter than the latter and, inversely, the latter are narrower and more branched than the former. Here, in order to detect the network of vessels, we are only interested in the main vessels.

The detection process is based on three morphological stages. First, a *gray-scale bottom-hat transformation* is used to enhance just the vessels. Second, an *iterative threshold binarization* is done to select the main vessels from the output image from the first stage. Finally, a post-processing stage is applied in order to refine the network of vessels obtained in the second stage.

A bottom-hat transformation is a morphological operation consisting of two steps: first, a morphological closing is applied to an input image and, second,

the input image is subtracted from the closing result. In our case, the closing is only applied to the green channel of the normalized and reduced input image, I_0 , and the result, I_c , is a new retinal image without vessels. We only used the green channel because there is experimental evidence in the literature about the high contrast between vessels and background for this channel [36]. Then the difference of the closing image and the original image produces the final output of this stage, $I_1 = I_c - I_0$, that is, a gray level image where only the vessels are enhanced. The *structuring element* used in the closing has a circular shape and its radius is calculated as the approximated mean of the maximum vessel diameters, $\bar{d}_{v_{max}}$, obtained from the DRIVE database [37] and considering the resolution K_0 . DRIVE is used here because the vessel network ground truth is publicly available on the web [38]. The value calculated for $\bar{d}_{v_{max}}$ at DRIVE original size (without applying the scale factor α) was $9 px$. Fig. 5(a-c) show an example of the different steps in this stage.

Subsequently, I_1 works as input to the iterative threshold binarization stage. Here a threshold is decremented progressively, $th_{i+1} = th_i - \varepsilon$, where $\varepsilon \gtrsim 0$ and $th_0 = \max(I_1)$. In each iteration, the threshold, th_i , is used to binarize I_1 , obtaining an iterative binary approach to the vessel network. As th_i becomes smaller, the number of vessels shown in the binary image is higher. The iterative process finishes when the value of the vessel area, A_v , is $\bar{A}_v^{Drive} < A_v < 1.1\bar{A}_v^{Drive}$, where \bar{A}_v^{Drive} is the average area of the network of vessels for all the images of the DRIVE database at resolution K_0 . The value calculated for \bar{A}_v^{Drive} at the DRIVE original size was 28,689 pixels. Fig. 5(d-f) show an example of the different steps in this stage.

Finally, a post-processing stage is applied to the second stage output, I_2 . Specifically, four operators are applied sequentially. First, a filtering is done to eliminate very small noisy blobs, using an area threshold as the filtering criterion ($th_{p1} = 0.01\bar{A}_v^{Drive}$). Second, a binary closing is applied to interconnect isolated vessel blobs. Next, a new filtering is done in order to eliminate blobs with no vessel aspect. Specifically, the blob filtering criterion is based on the simultaneous fulfillment of three properties related to the blob geometric properties: (i) the ratio between the blob area and its bounding box is greater than a threshold ($th_{p2} = 0.2$); (ii) the ratio between the blob area and the square area of side Δx_{bb} is greater than a threshold ($th_{p3} = 0.2$), where Δx_{bb} is the x-component of the blob bounding box; and (iii) the blob area is less than a threshold ($th_{p3} = 0.5\bar{A}_v^{Drive}$). The first property is used to filter noisy blobs associated with exudates and cotton wool spots; the second one, to filter horizontally elongated blobs (secondary vessels); and, the third one, to filter medium or small blobs. Using knowledge of the domain, an initial value was chosen for each parameter th_{p1} , th_{p2} and th_{p3} . Then, different experiments were carried out in order to select the best values from a set of values close to the initial values. Finally, a binary AND operation, between the last filtering operator output and I_2 , is done in order to eliminate the closing bloat effect but preserving the filtering effects. Fig. 5(g-i) show an example of the different steps in this stage. To summarize, the block diagram in Fig. 6 shows the entire process, where the three stages mentioned above are included.

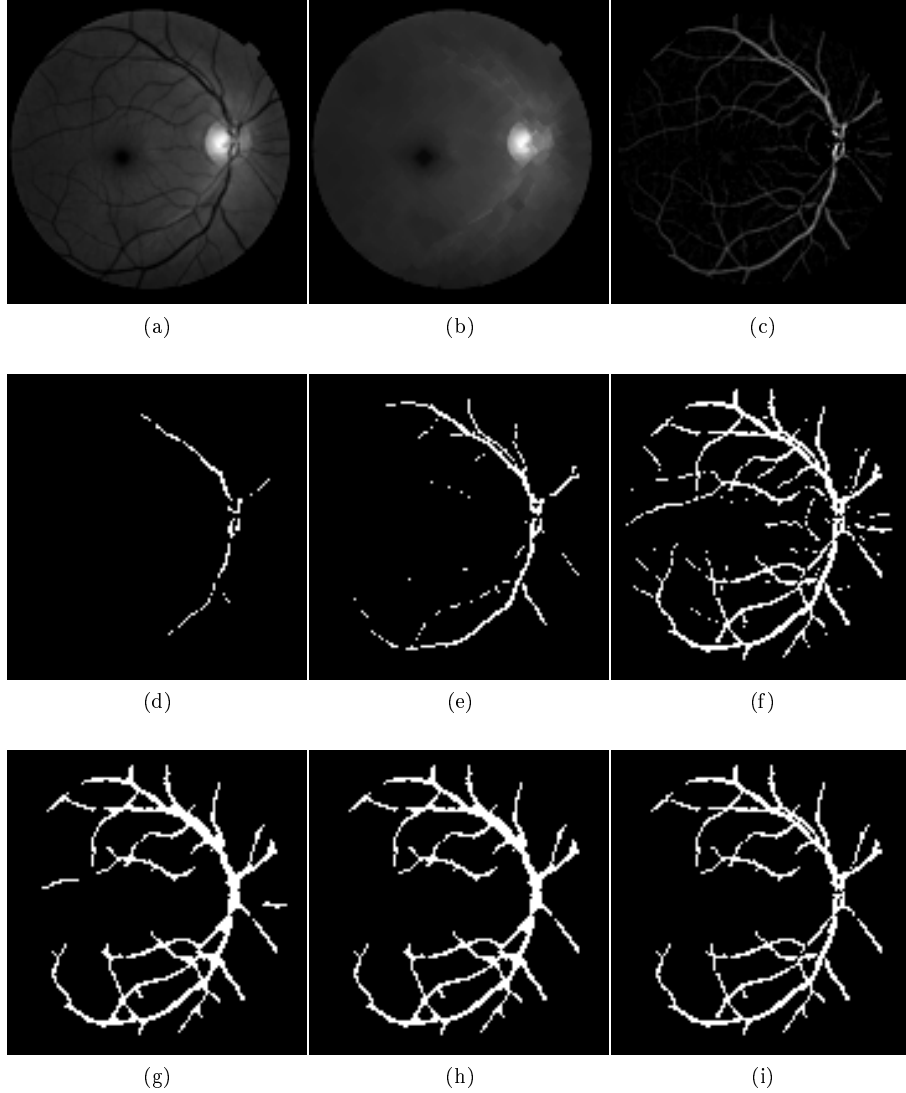


Figure 5: Example of vessel blob detection using three stages: bottom-hat transformation (1st row), iterative threshold binarization (2nd row) and post-processing stage (3rd row): (a) I_0 , green channel of normalized and reduced image (input image); (b) I_c , morphological closing of I_0 ; (c) $I_1 = I_c - I_0$, gray level vessel network (output of first stage); (d-e) results of applying an iterative threshold, th_i , to I_1 ; (f) I_2 , first approach to the binary vessel network (output of the second stage); (g) filtering and closing of I_2 ; (h) filtering of blobs with no vessel aspect; (i) undoing closing (final vessel network).

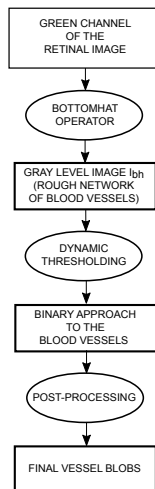


Figure 6: Block diagram illustrating the three stages used in the process of detecting the network of the main blood vessels.

3.2.4. Vascular bundle blob detection

In a retinal image, the vascular bundle is formed by the vessels that are located within of the OD [39]. The point linking the superior (nasal and temporal) and inferior (nasal and temporal) arcade, which emerge from the OD, is called the *center of the vascular bundle*. This point is located near the OD center (see Fig. 1).

The detection of the vascular bundle candidate blobs is done by means of TM with correlation. However, unlike the optic disc and macula, TM is not applied to RGB retinal images. It is applied to vessel network images obtained with the method described in the previous section. In addition, since the orientation of vessels emerging from the vascular bundle is different in the left and right eye, a vascular bundle template is created for each type of eye. The n_{vb} brightest blobs per type of eye in the TM output are chosen, giving a total of $N_{vb} = 2 \times n_{vb}$ candidate vascular bundle blobs, where n_{vb} is chosen by the user.

The two templates were chosen with a square shape. Due to the fact that the vascular bundle center ground truth is not available, first at all, an auxiliary template matrix for right eye was calculated as the intensity average of different square sub-windows, with width $W' = 11R_{OD}$, where R_{OD} is obtained from eq. (2). These sub-windows are extracted from vessel network binary images and centered on the actual geometric center of the optic disc. We choose a value of W' large enough as to define a sub-window that contains and distinguishes the initial part of the four arcades that emerge from the vascular bundle (superior/inferior and nasal/temporal). However, the actual location of the vascular bundle center is normally slightly offset from the OD center (see, for example, Fig. 1). Therefore, the final template is obtained by extracting a square sub-window from the above auxiliary template and centered visually in the vascular

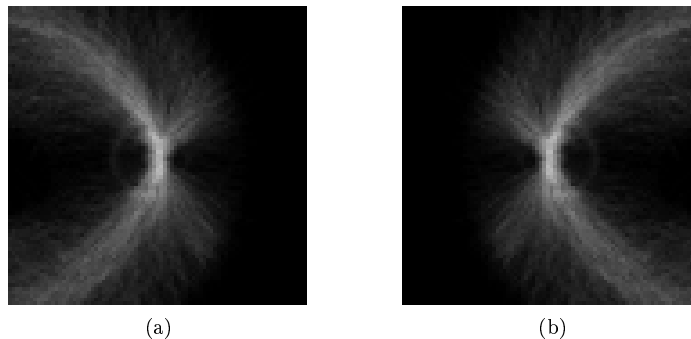


Figure 7: Vascular bundle templates used for each type of eye: (a) right eye; (b) left eye.

bundle center. To do this, the final size of the new sub-window, W_{VB} , has to be slightly smaller than W' (we choose $W_{VB} = 10R_{OD}$). The vessel network images used here are the result of applying the method of vessel blob detection (see section 3.2.3) to different MESSIDOR images. Specifically, 200 non-pathological images of the right eye were used. In addition, the template of the left eye was obtained by horizontally mirroring the previous one. Fig. 7 shows the two final vascular bundle templates used (left and right eye).

Finally, as a summary, Fig. 8 shows the information flow of the intra-SRK stages used for obtaining the sets of candidate blobs for the different anatomical structures.

3.3. Using inter-structure relational knowledge

One of the main contributions of our methodology is the use of inter-structure relational knowledge in order to eliminate false positive candidate blobs and simultaneously detect the different anatomical structures (true positives): optic disc (OD), macula (M), and vascular bundle (VB). Thus, different relations between the main retinal anatomical structures are used:

- R_1 : The OD geometric center is located inside the OD area where there always exists a high accumulation of vessels (see Fig. 1).
- R_2 : The macula center (fovea) lies in an avascular region [5].
- R_3 : The VB center is a point of vessel, surrounded by more vessels, located inside the OD area, and very close to the OD geometric center (see Fig. 1).
- R_4 : The center of the fovea is usually located at a distance of approximately 2.5 times the diameter of the OD, from the center of the OD [17]. This distance is denoted by $\tilde{D}(OD, F)$ and can also be expressed in terms of OD radii as:

$$\tilde{D}(OD, F) = 5R_{OD} \quad (3)$$

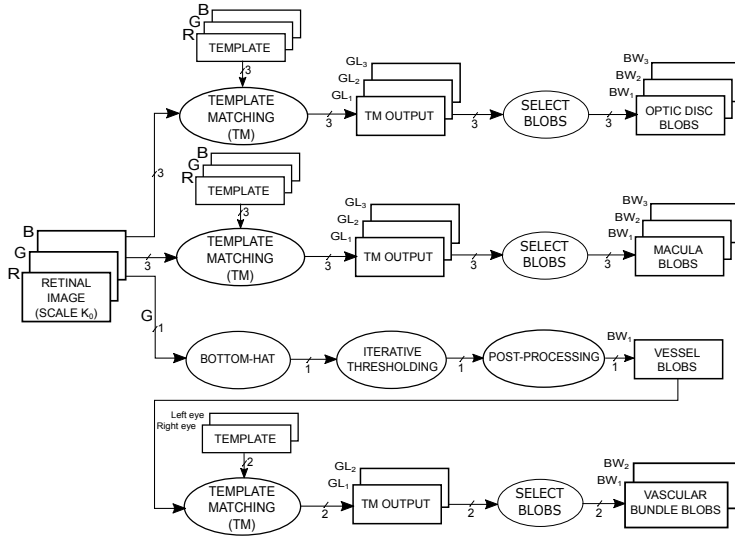


Figure 8: Block diagram showing the different stages used for obtaining the different sets of candidate blobs: optic disc, macula, vessels and vascular bundle. The color channels are represented by R (red), G (green) and B (blue); the gray level images are represented by GL_i ; and black and white images (binary images) are represented by BW_i .

- R_5 : In the right eye, the VB and the OD are always located on the right of the macula (see Fig. 1). The opposite occurs in the left eye.
- R_6 : In the right eye, the VB center is normally located on the right of the OD geometric center (see Fig. 1). The opposite occurs in the left eye.

The above inter-SRK will be used to select the best triplet, (B_{OD}, B_M, B_{VB}) . Thus, assuming that N_{OD} , N_M and N_{VB} are, respectively, the total number of OD, macula and VB candidate blobs, the selection algorithm of the best triplet is implemented as follows:

1. Discarding false positive OD blobs: every OD blob whose geometric center is located at a distance greater than a threshold value from any retinal vessel is discarded (see relation R_1). We take one R_{OD} , see eq. (2), as the threshold value. Next N_{OD} is updated appropriately.
2. Discarding false positive macula blobs: every macula blob whose geometric center is located at a distance less than a threshold value from any retinal vessel is discarded (see relation R_2). We take $(1/4)R_{OD}$ as the threshold value. Next N_M is updated appropriately.
3. Discarding false positive VB blobs: every VB blob whose geometric center is located at a distance greater than a threshold value from any retinal vessel is discarded (see relation R_3). We take one R_{OD} as the threshold value. Next N_{VB} is updated appropriately.

4. With the remaining blobs, a set containing all the possible triplets is formed, $(B_{OD_i}, B_{M_j}, B_{VB_k})$, where $i = 1, \dots, N_{OD}$, $j = 1, \dots, N_M$ and $k = 1, \dots, N_{VB}$.
5. Discarding false positive triplets. Every triplet whose couple of blobs verifies any of the following conditions is discarded from the set of triplets:
 - (a) $D(B_{OD_i}, B_{VB_k}) > 2R_{OD}$, that is, the distance between the OD and VB blob geometric centers is greater than a threshold value. We take $2R_{OD}$ as the threshold because it is the maximum allowable distance considering that the OD and VB have to be inside the OD area (see relations R_1 and R_3).
 - (b) $\left| D(B_{OD_i}, B_{M_j}) - \tilde{D}(OD, F) \right| > 2R_{OD}$, where $|\cdot|$ is the absolute value operator, $D(B_{OD_i}, B_{M_j})$ is the distance between the OD and macula blob geometric centers, and $\tilde{D}(OD, F)$ is obtained from the relation R_4 . We take $2R_{OD}$ as the threshold value because the worst case corresponds to the case in which OD and macula blobs have a deviation of one R_{OD} in relation to their respective actual locations and they are located in opposite positions.
 - (c) $\left| D(B_{M_j}, B_{VB_k}) - \tilde{D}(OD, F) \right| > 2R_{OD}$, where $D(B_{M_j}, B_{VB_k})$ is the distance between the macula and VB blob geometric centers, and $\tilde{D}(OD, F)$ is obtained from the relation R_4 . This condition is a consequence of the proximity of the actual OD and VB centers (see relation R_3). So, we take $2R_{OD}$ as the threshold for the same reason explained in the previous case.
 - (d) The macula blob is located on the left of a left VB blob. Inversely, the macula blob is located on the right of a right VB blob. Both conditions are a consequence of R_5 .
 - (e) The OD blob is located on the left of a left VB blob and at a distance higher than one R_{OD} . Inversely, the OD blob is located on the right of a right VB blob and at a distance higher than one R_{OD} . This condition is a consequence of relations R_3 and R_6 .
6. If the final set of triplets obtained in step 5 is not empty, the following fitness function is applied to each triplet:

$$F(B_{OD_i}, B_{M_j}, B_{VB_k}) = F_1(B_{OD_i}, B_{M_j}) + F_2(B_{M_j}, B_{VB_k}) + F_3(B_{OD_i}, B_{VB_k}) \quad (4)$$

with

$$F_1(B_{OD_i}, B_{M_j}) = \frac{I_{TM}(B_{OD_i}) \cdot I_{TM}(B_{M_j})}{1 + \frac{|D(B_{OD_i}, B_{M_j}) - \tilde{D}(OD, F)|}{2R_{OD}}} \quad (5)$$

$$F_2(B_{M_j}, B_{VB_k}) = \frac{I_{TM}(B_{M_j}) \cdot I_{TM}(B_{VB_k})}{1 + \frac{|D(B_{M_j}, B_{VB_k}) - \tilde{D}(OD, F)|}{2R_{OD}}} \quad (6)$$

$$F_3(B_{OD_i}, B_{VB_k}) = \frac{I_{TM}(B_{OD_i}) \cdot I_{TM}(B_{VB_k})}{1 + \left[\frac{D(B_{OD_i}, B_{VB_k})}{2R_{OD}} \right]} \quad (7)$$

where $I_{TM}(B_{x_i})$ is the gray-level intensity of the TM output for the i -th blob of type x , and $|\cdot|$ is the absolute value operator. Then the triplet that obtains maximum fitness will be the solution to the three anatomical structures:

$$(B_{OD}, B_M, B_{VB}) = \arg \max_{x \in \mathbf{B}} F(x) \quad (8)$$

where $\mathbf{B} = \{(B_{OD_i}, B_{M_j}, B_{VB_k}), \forall i, j, k\}$. Note that, in eqs. (5), (6) and (7), the denominators are normalized by $2R_{OD}$, and the numerators are scaled to $[-1, +1]$ due to the fact the template matching used is based on normalized cross-correlation.

7. In the other case (the set of triplets is empty), we return to step 4, but now considering all possible couples, (B_{OD_i}, B_{M_j}) , (B_{M_j}, B_{VB_k}) and (B_{OD_i}, B_{VB_k}) . Next false positive couples are discarded according to the rules expressed in step 5. Then each type of couple is evaluated, respectively, according to fitness functions (5), (6) and (7). After that, the best couple is selected according to the criterion of maximum fitness for each type of couple:

$$(B_{OD}^1, B_M^1) = \arg \max_{x \in \mathbf{B}_1} F_1(x)$$

$$(B_M^2, B_{VB}^2) = \arg \max_{x \in \mathbf{B}_2} F_2(x)$$

$$(B_{OD}^3, B_{VB}^3) = \arg \max_{x \in \mathbf{B}_3} F_3(x)$$

where:

$$\begin{aligned} \mathbf{B}_1 &= \{(B_{OD_i}, B_{M_j}), \forall i, j\} \\ \mathbf{B}_2 &= \{(B_{M_j}, B_{VB_k}), \forall j, k\} \\ \mathbf{B}_3 &= \{(B_{OD_i}, B_{VB_k}), \forall i, k\} \end{aligned}$$

In this step, each type of blob can appear in two of the three winning couples or, in the worst case, \mathbf{B}_1 , \mathbf{B}_2 and \mathbf{B}_3 can be empty sets. To address this variety of cases, the solution blob for each structure is chosen according to eqs. (9), (10) and (11).

$$B_{OD} = \begin{cases} \arg \max_{x=B_{OD}^1, y=B_{OD}^3} \{F_1(x, B_M^1), F_3(y, B_{VB}^3)\}, & \text{if } \mathbf{B}_1 \cup \mathbf{B}_3 \neq \emptyset \\ \arg \max_{x \in B_{OD_i}} I_{TM}(x) & \text{other case} \end{cases} \quad (9)$$

$$B_M = \begin{cases} \arg \max_{x=B_M^1, y=B_M^2} \{F_1(B_{OD}^1, x), F_2(y, B_{VB}^2)\} & \text{if } \mathbf{B}_1 \cup \mathbf{B}_2 \neq \emptyset \\ \arg \max_{x \in B_{M_j}} I_{TM}(x) & \text{other case} \end{cases} \quad (10)$$

$$B_{VB} = \begin{cases} \arg \max_{x=B_{VB}^2, y=B_{VB}^3} \{F_2(B_M^2, x), F_3(B_{OD}^3, y)\} & \text{if } \mathbf{B}_2 \cup \mathbf{B}_3 \neq \emptyset \\ \arg \max_{x \in B_{VB_k}} I_{TM}(x) & \text{other case} \end{cases} \quad (11)$$

4. Experimental Results

The final value chosen in all experiments for the standard resolution was $K_0 = 9 \text{ px/mm}$. The scale factor value, α , needed to transform each image to K_0 , is calculated using eq. (1). The K_0 value was chosen following the trade-off of being small enough to remove noisy artifacts from the original image and large enough not to hinder the detection of the searched structures. In any case, this value is not critical and any other similar value could have been chosen. For all experiments, the number of candidate blobs was $N_{OD} = 9$ for optic disc ($n_{od} = 3$, i.e. three blobs per each RGB channel), $N_M = 9$ for macula blobs ($n_m = 3$), and $N_{VB} = 4$ for vascular bundle ($n_{vb} = 2$, i.e. two per each type of eye). These values were obtained experimentally, taking into account that lower values might not include the solution blob in the set of candidate blobs and, inversely, higher values could increase the processing time of the method.

To determine our evaluation criteria we have considered those used in the literature. As in most papers [4, 24, 27, 40], we consider a successful criterion for OD detection if the distance from the estimated OD center to the real OD center is less than or equal to one OD radius. Regarding the macula, most of the research works have used the distance to the macula center as a reference point. Thus macula detection will be successful if the distance from the estimated macula center to the real macula center is less than or equal to p times one OD radius. Here, depending on the approach considered, the value of p can be different. For example, $p = 1/2$ in [27], $p = 1$ in [5, 34], or $p = 2$ in [24]. Finally, in relation to the vascular bundle, a successful detection is considered if the distance from the estimated vascular bundle center to the real OD center is less than or equal to one OD radius. We chose the real OD center as a reference because it is always close to the center of the vascular bundle (see Fig. 1).

4.1. MESSIDOR database

For the first experiment, the MESSIDOR database is used. In order to make a fair comparison, our method should be compared with other methods that detect and evaluate the same three structures detected and evaluated by our method. However it was not possible because such methods do not exist. In any case, Table 2 shows a comparison of our method with other research in terms of OD and/or macula detection success rate.

On the other hand, it is also important to evaluate how retinopathy affects the performance of our method. Thus, Tables 3 and 4 show, respectively, a comparison of OD and macula detection success rates of our method with other approaches in the literature considering different retinopathy grades and different risks of macular edema in the MESSIDOR database.

Table 2: Comparison of optic disc (OD) and macula detection success rates (expressed in %) with other methodologies in the literature. Results are shown as presented in the papers where methodologies are published. In order to facilitate the comparison with [9, 26], the values shown are the result of combining the two results of normal and pathological image sets into one unique result. Note that each database is formed by normal (norm) and pathological (path) images.

Method	Database	#Images (norm+path)	OD	Macula (p)		
				($\frac{1}{2}$ R)	(1R)	(2R)
Fleming et al. [25]	Private	1056	98.40	-	96.50	98.50
Tobin et al. [24]	Private	345 (18+327)	90.04	-	-	92.50
Niemeijer et al. [9]	Private	600 (500+100)	97.67	-	94.00	-
Niemeijer et al. [26]	Private	549 (449+100)	98.23	-	95.38	-
Yu et al. [27]	MESSIDOR	1200 (546+654)	98.33	95.00	-	-
Gegundez et al. [4]	MESSIDOR	1200 (546+654)	99.00	96.08	96.92	97.83
Giachetti et al. [5]	MESSIDOR	1200 (546+654)	99.66	-	99.10	-
Aquino [34]	MESSIDOR	1136 (533+603)	-	91.28	98.24	99.56
Kao et al. [22]	MESSIDOR	1200 (546+654)	-	97.83	98.17	-
Marin et al. [16]	MESSIDOR	1200 (546+654)	99.75	-	-	-
Girard et al. [41]	MESSIDOR	1200 (546+654)	-	94.00	98.00	-
Dashtbozorg et al. [23]	MESSIDOR	1200 (546+654)	99.75	93.75	98.87	99.58
This work	MESSIDOR	1200 (546+654)	99.33	96.08	98.58	99.50

Table 3: Comparison of optic disc detection success rates (expressed in %) with previous works for different retinopathy and risk of macular edema grades in the MESSIDOR dataset. Results are shown as presented in the papers where methodologies are published.

Method	Retinopathy grade				Risk of macular edema				
	0	1	2	3	Any	0	1	2	Any
Yu et al. [27]	98.71	99.34	99.19	96.16	98.33	98.39	100	97.26	98.33
Giachetti et al. [5]	99.62	100	100	99.23	99.66	99.69	100	99.35	99.66
This work	99.08	99.35	100	99.21	99.33	99.28	100	99.34	99.33

Table 4: Comparison of macula detection success rates (expressed in %) with previous works for different retinopathy and risk of macular edema grades in the MESSIDOR database. Results are shown as presented in the papers where methodologies are published, except for those shown in [4] which are obtained from [5]. Our method is tested for two criteria (p): $1R$ and $\frac{1}{2}R$, in order to compare different approaches.

Method	p	Retinopathy grade					Risk of macular edema			
		0	1	2	3	Any	0	1	2	Any
Giachetti et al. [5]	$1R$	99.80	100	99.20	98.70	99.10	99.40	100	96.90	99.10
Gegundez et al. [4]	$1R$	99.20	98.70	99.10	95.40	98.20	98.80	98.60	95.80	98.20
This work	$1R$	99.63	100	98.79	95.28	98.58	99.18	100	94.04	98.58
Yu et al. [27]	$\frac{1}{2}R$	97.78	99.35	95.95	85.77	95.00	96.19	98.67	85.71	95.00
This work	$\frac{1}{2}R$	97.62	100	97.57	88.98	96.08	97.33	100	86.09	96.08

4.2. Other public databases

In order to provide evidence about the robustness of our methodology, other public databases were used: DRIONS, ONHSD and DIARETDB1. Here, it is important to note that, with these databases, the method was evaluated using the same parameter configuration as that one used with the MESSIDOR database. Table 5 shows the success rates obtained. Note that the DRIONS database has the peculiarity of not showing the macular area in most of its images, so the method is only evaluated for OD and VB.

In summary, considering the results obtained in the four databases, the overall success rate for a structure s , denoted by $SR_{ov}(s)$, can be computed from eq. (12), where DB_i is the i -th database, $size_{DB_i}$ is the number of images in the DB_i , $SR_{DB_i}(s)$ is the success rate accomplished by the method in the DB_i for s , and n is the number of different databases in which s was searched. Thus, the overall success rate for each structure in this study was: 99.26% (OD), 98.69% (macula) and 98.95% (vascular bundle).

$$SR_{ov}(s) = \frac{\sum_{i=1}^n size_{DB_i} \times SR_{DB_i}(s)}{\sum_{i=1}^n size_{DB_i}} \quad (12)$$

Finally, Fig. 9 shows two examples (1st and 2nd column) with intermediate outputs of the detection process. Specifically, Fig. 9(a,c,e) show an example of successful detection of the three structures and Fig. 9(b,d,f) show another example in which the OD and the VB are correctly detected but not the macula.

5. Discussion

To the best of our knowledge, there not exist works in the literature that address the detection and evaluation of the three structures detected here (OD, macula and vascular bundle). Therefore, we can only compare our results with other approaches where two or less anatomical structures are detected and evaluated. As can be seen in the above section, the success rates obtained with

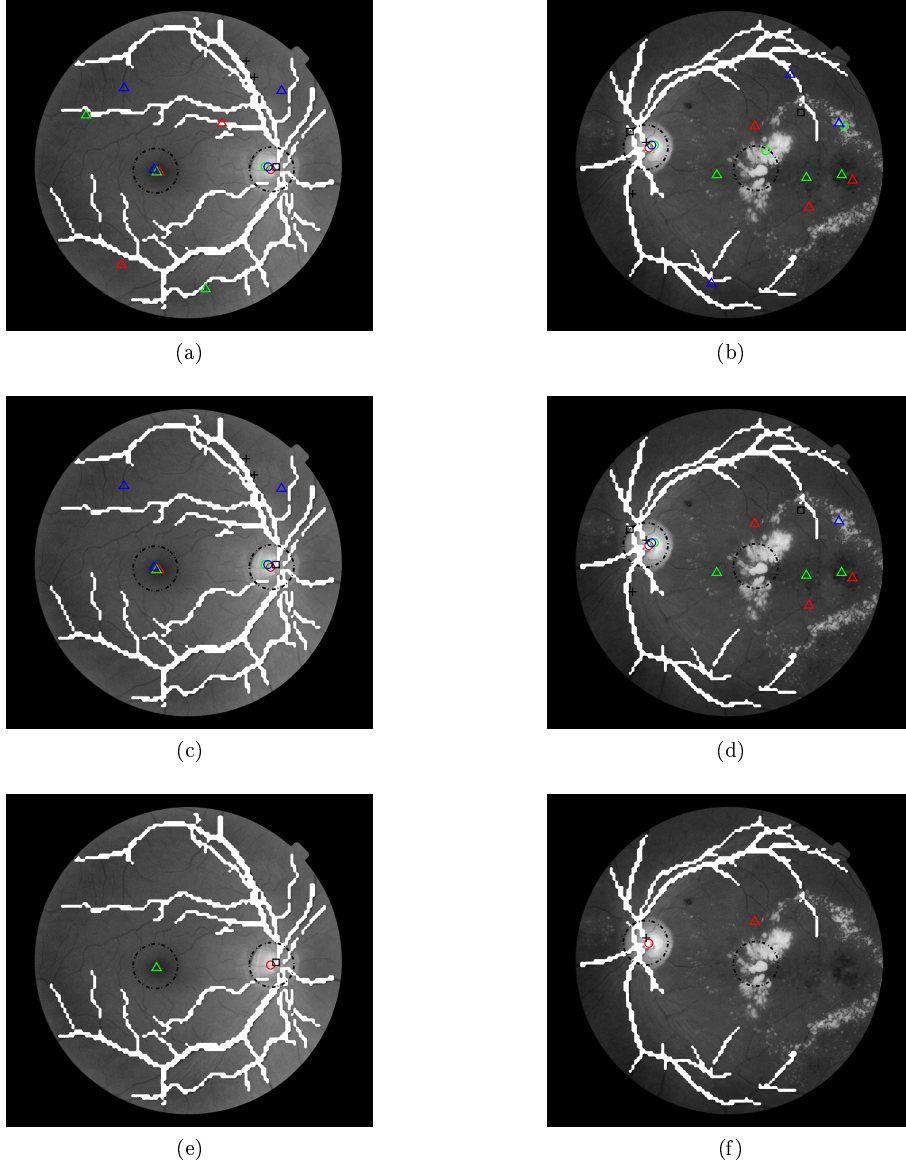


Figure 9: Two examples with intermediate outputs of the detection process: successful detection (1st column) and erroneous detection in macula (2nd column). The first row shows the set of candidate blobs for each structure (see Section 3.2). The second row shows the result of filtering blobs according to steps 1-3 of the triplet selection algorithm (see Section 3.3). The third row shows the solution blobs (step 6 or 7 of triplet selection algorithm). Circles, triangles, squares and crosses represent OD, macula, right and left VB blobs, respectively (in the online version, each color is associated with its respective RGB channel). Dashed circumferences (radius= $1R_{OD}$) are centered in the OD and macula actual centers.

Table 5: Comparison of OD, macula and VB detection success rates (expressed in %) in other public databases and different to the MESSIDOR database.

Method	Database	# Images	OD	Macula ($p=1R$)	VB
Mahfouz and Fahmy [2]	DIARETDB1	89	97.75	-	97.75
Welfer et al. [21]	DIARETDB1	89	-	92.13	-
Cao et al. [11]	DIARETDB1	89	97.75	-	97.75
Aquino [34]	DIARETDB1	89	-	94.38	-
Kao et al. [22]	DIARETDB1	89	-	94.38	-
Medhi and Dandapat [10]	DIARETDB1	89	-	95.51	-
Xiong and Li [19]	DIARETDB1	89	97.75	-	-
Mittal and Sivaswamy [7]	DIARETDB1	89	97.75	96.00	-
This work	DIARETDB1	89	96.63	100	97.75
Lowell et al. [12]	ONHSD	87	100	-	-
This work	ONHSD	87	100	98.85	97.70
Molina and Carmona [42]	DRIONS	110	100	-	-
This work	DRIONS	110	100	-	100

our method are competitive in relation to other recent approaches tested on the MESSIDOR database (see Table 2). Specifically, our OD and macula detection results are, respectively, 99.33% and [96.08% ($p = 1/2$), 98.58 ($p = 1$), 99.50% ($p = 2$)]. If the entire available results for each approach are used, our results are only slightly surpassed by two methods [5, 16]. Thus, in [5], the OD and macula are detected with a success rate of, respectively, 99.66% and 99.10% ($p = 1$), but the macula detection results for $p = 1/2$ and $p = 2$ are not available and they were obtained for 1136 out of 1200 MESSIDOR images. Otherwise, in [16], the OD success rate is 99.75%, but it is the only structure detected and evaluated. Good OD and macula detection results are obtained in [23] (99.75% and [93.75% ($p = 1/2$), 98.87% ($p = 1$), 99.58% ($p = 2$)], but our success rate for $p = 1/2$ is slightly higher (96.08%). The OD and macula detection is addressed in [22], but only macula success rates are provided [97.83% ($p = 1/2$), 98.17% ($p = 1$)], obtaining the highest success rate for $p = 1/2$ in relation to the entire approaches used in our comparative study (our success rate for $p = 1/2$ is the second best). The results obtained in [41] are interesting because they also simultaneously detect the OD and macula. First, they detect OD-macula candidate pairs and then they select the best pair. However, their macula detection results [94.0% ($p = 1/2$), 98.0% ($p = 1$)] are slightly lower and their OD segmentation and our OD detection results are not comparable. Finally, our OD and macula detection results equal or slightly outperform those obtained in [4, 27] and outperform those achieved in [9, 24, 25, 26].

The discussion of the vascular bundle results is less direct. On the one hand, there exist approaches that combine convergence of blood vessels with detection of other patterns in order to finally detect the OD (see, for example, [9, 16]). In these cases, we think that our OD detection results (not our vascular bundle

detection results) should be used to compare with the results obtained in this kind of approaches (see Table 2). On the other hand, there are other approaches that directly search the center of the vascular bundle as the OD center [2, 11]. In these cases, the detection results obtained could be more directly comparable with our vascular bundle detection results. Thus the vascular bundle success rate obtained by our method (97.75%) equals to that one obtained in [2] and [11] for the DIARETDB1 database (see Table 5). In each of the two mentioned references, three more databases are used, but these are different to those ones used in our experiments. However, we can still compare the average vascular bundle success rate considering the four databases used in each study. In this case, our result (98.3%) is slightly better than that one obtained in [2] and [11] with a average success rate of 97.0% and 96.6%, respectively.

The presence of typical visual patterns associated with two important retinal pathologies is also analyzed. Thus, Tables 3 and 4 show the influence of the degree of diabetic retinopathy (DRG) and the risk of macular edema (RME) in the detection results. The DRG is expressed as a function of the number of microaneurysms (μA), number of hemorrhages (H) and neovascularization ($NV = 1$), where the meaning of the different grades are: "0 (Normal)" $\rightarrow (\mu A = 0) \wedge (H = 0)$; "1" $\rightarrow (0 < \mu A \leq 5) \wedge (H = 0)$; "2" $\rightarrow [(5 < \mu A < 15) \vee (0 < H < 5)] \wedge (NV = 0)$; and "3" $\rightarrow (\mu A \geq 15) \vee (H \geq 5) \vee (NV = 1)$. The RME is expressed in terms of the presence or absence of hard exudates (hE): "0 (No risk)" \rightarrow "No visible hE "; "1" $\rightarrow \min_distance(\text{macula}, hE) > 2R_{OD}$; and "2" $\rightarrow \min_distance(\text{macula}, hE) \leq 2R_{OD}$. In relation to the OD, the detection successes are always higher than 99%, regardless of the DRG or RME. In any case, errors are obtained in images with advanced peripapillary atrophies or posterior staphylomas (signs not considered for DRG or RME). Regarding the macula ($p = 1$), the method obtains a success percentage higher than or equal to 99% in images with $DRG = \{0, 1, 2\}$ or $RME = \{0, 1\}$. However this percentage drops to 95.28% in those images with a high number of microaneurysms or hemorrhages ($DRG = 3$) and falls to 94.04% in those images with large hard exudates in the macular area ($RME = 2$), for example, see Fig. 9(f). With respect to the vascular bundle, the method can fail in images where the main vessels emerging from the OD center do not follow the typical curved pattern shown in Fig. 7 (the path is straight up and down or has a reverse curvature). In these cases, the detection mark is attached to a vessel point located outside the OD but very close to its upper or lower boundary. Finally, in relation to illumination conditions, the method is robust to non-homogenous illumination and only partially affected (error in one or two of the three structures) when there are serious illumination problems in the image.

In relation to other databases, the detection results obtained for the different structures are also competitive and consistent with the results obtained in the MESSIDOR database (see Table 5). In particular, our macula detection result in DIARETDB1 (100%, $p = 1$) is the highest in relation to all other approaches with which we compare. From a global point of view, these results support and reinforce the hypothesis that our method is robust and independent of the database considered.

Table 6: Success rate (expressed in %) in the MESSIDOR database for each anatomical structure depending on the amount of inter-SRK injected in the search process.

Anatomical structure	No inter-SRK $\max\{I_{TM}(B_x)\}$	inter-SRK for couples	inter-SRK for triplets
Optic disc	98.00	98.25	99.33
Macula ($p = 1R$)	97.08	98.41	98.58
Vascular bundle	96.58	97.17	97.92
Average	97.22	97.94	98.61

A study was also done of how the amount of inter-SRK used affects the selecting process of the best tuple. Table 6 shows the results obtained in the MESSIDOR database. Thus, for example, in the first experiment, the inter-SRK is not used at all and the highest response template matching of each type of structure is selected as the solution, $\max(I_{TM}(B_x))$, where B_x is a blob of type- x and $x \in \{od_i, m_j, vb_k\}$. The results for this case are shown in the second column and they are worse than those obtained with the original method (fourth column). Next, in the second experiment, inter-SRK is used but considering couples of structures, that is, non triplets as in the original method. Here, the algorithm used is the same as the one mentioned in section 3.3, but without applying steps 5 and 6. The results are shown in the third column. Compared with the previous case, the use of inter-two-structure relational knowledge improves the percentages of successes, but the results are worse than those of the original method where all the available inter-SRK is used.

Other similar study can be done considering a successful criterion for detection if the three detected structures correspond simultaneously to three true positives. The success rates obtained in the MESSIDOR database were the following: 91.91% if the highest TM response of each type of structure is selected as the solution (inter-SRK is not used), 94.17% if only inter-two-SRK is considered, and 95.91% if the original method (triplets) is used. Once again, the detection process improves as the amount of inter-SRK increases.

The use of the two VB templates (right and left) has an additional advantage. They allow us to distinguish whether the image corresponds to right or left eye. Thus, if we select in each image the VB blob with maximum template matching response, its template associated always matches the type of eye in the 1200 MESSIDOR images. Therefore, these two templates could be used separately as a fast and simple method of identifying the type of eye.

We consider that one advantage of the proposed methodology is the use of two stages in each of which a different type of knowledge (intra- and inter-SRK) is used. This allows us to simplify the detection methods used in the first stage because we are only interested in detecting candidate blobs for each structure. The second stage only has to use the inter-SRK in order to select the best candidate tuple. In contrast, there are other approaches in the literature that assume the final detection of each structure separately from the beginning (for

Table 7: Comparison with competitive methods in the literature considering the hardware, programming language, the computation time and the number and type of structure detected: Optic Disc (OD), Macula (M), Main Vessels (V) and Vascular Bundle (VB).

Method	Hardware	Language	Time (s)	#Structures detected (type)
Fleming et al. [25]	Intel Pentium 4, 2.4GHz	MATLAB & C	120	3 (OD, M, V)
Niemeijer et al. [9]	Intel Pentium 4, 3GHz	C++	600	3 (OD, M, V)
Niemeijer et al. [26]	Intel Core 2 Duo, 2.83GHz	C++	27.6	3 (OD, M, V)
Yu et al. [27]	Intel Xeon W3520, 2.67GHz, 6GB RAM	MATLAB	3.9	2 (OD, M)
Giachetti et al. [5]	Intel Core i7 Q 740, 2.93GHz	MATLAB	5	3 (OD, M, V)
Kao et al. [22]	Intel Core i7-3610QM, 2.30GHz	C++	[2.6,6.9]	2 (OD, M)
Marin et al. [16]	Intel Xeon 3.2 GHz, 32GB RAM	MATLAB	5.42 ± 0.98	2 (OD, V)
Mittal and Sivaswamy [7]	2.1 GHz, 4GB RAM	MATLAB	[120,160]	2 (OD, M)
This work	Intel Core i7-2640M, 2.8 GHz, 8GB RAM	MATLAB	4.16 ± 0.72	4 (OD, M, V, VB)

example, see [17]) or the prior detection of a structure to be used as a reference in the detection of a second one [4, 24, 25, 27]. In both cases, the approaches used are more complex and have more computational cost than the methodology presented here. In this sense, several aspects related to implementation and computational cost can also be considered. The method was implemented with MATLAB language, in a laptop with CPU Intel Core i7-2640M, 2.8GHz and 8GB RAM. Table 7 shows a comparison of our approach with other methods in the literature. As these algorithms were implemented in different computer system, the run-time should be interpreted in function of the number of structures detected and the hardware and programming language used. In any case, for a fair comparison, the table only shows the results of those research works in which two or more structures are detected. Our method is fast, considering that four structures are detected simultaneously and an interpreted language is used. It could be even faster if a compiled language was used.

6. Conclusions and Future work

In this paper, we have presented a methodology for the detection of the main anatomical structures in retinal images. This methodology is independent of the original image size and uses two types of relational knowledge: intra- and

inter-structure. The first type has been commonly used in the related literature. However, the second type has normally been used after prior detection of one or more structures obtained independently. In our approach, the inter-structure relational knowledge is used for the simultaneous detection of the main retinal structures. The main advantage of that simultaneous detection was the reduction of the number of false positives in the detection process.

A method was implemented based on the mentioned methodology. It is fast, simple and its detection results are competitive in relation to other methods existing in the recent literature. Unlike other approaches dedicated to detect one structure, our method is able to simultaneously detect four different anatomical structures (optic disc, macula, network of vessels and vascular bundle). Maintaining the same parameter configuration, the method was applied to different public databases and, in all of them, the detection success rates obtained were consistent, providing evidence about its robustness.

As future work, the detection method could be applied as a prior step to the segmentation stage, in order to increase performance and reduce the computation time in such a stage. Finally, the proposed methodology could also be used in other types of images, related to both medical (for example, detection of anatomical structures and/or organs in digital radiography or resonance magnetic images) and non-medical domains (for example, detection of types of electronic components in board circuit images). In both cases, it is assumed that there is always topological information, related to the types of structures to detect, in order to be used as inter-SRK.

Conflict of interest

The authors declare that they have no conflicts of interest.

Acknowledgments

The authors would like to thank the MESSIDOR, DRIONS, ONHSD and DIARETDB1 program partners for facilitating their databases. We would also like to express our gratitude to Gegundez-Arias et al. [4] and Aquino [34] for allowing us to access their respective MESSIDOR and DIARETDB1 fovea ground truth.

References

- [1] M.H. Haleem, L. Han, J. van Hemert, and B. Li. Automatic extraction of retinal features from colour retinal images for glaucoma diagnosis: A review. *Comput. Med. Imag. Grap.*, 37(7–8):581–596, 2013.
- [2] A.E. Mahfouz and A.S. Fahmy. Fast localization of the optic disc using projection of image features. *Trans. Img. Proc.*, 19(12):3285–3289, 2010.

- [3] H. Yu, E.S. Barriga, C. Agurto, S. Echegaray, M.S. Pattichis, W. Bauman, and P. Soliz. Fast localization and segmentation of optic disk in retinal images using directional matched filtering and level sets. *IEEE T. Inf. Technol. B.*, 16(4):644–657, 2012.
- [4] M.E. Gegundez, D. Marin, J.M. Bravo, and A. Suero. Locating the fovea center position in digital fundus images using thresholding and feature extraction techniques. *Comput. Med. Imag. Grap.*, 37:386–393, 2013. doi: <http://dx.doi.org/10.1016/j.compmedimag.2013.06.002>.
- [5] A. Giachetti, L. Ballerini, E. Trucco, and P.J. Wilson. The use of radial symmetry to localize retinal landmarks. *Comput. Med. Imag. Grap.*, 37:369–376, 2013. doi: <http://dx.doi.org/10.1016/j.compmedimag.2013.06.005>.
- [6] M. Foracchia, E. Grisan, and A. Ruggeri. Detection of optic disc in retinal images by means of a geometrical model of vessel structure. *IEEE T. Med. Imaging*, 23(10):1189–1195, 2004. doi: 10.1109/TMI.2004.829331.
- [7] G. Mittal and J. Sivaswamy. Optic disk and macula detection from retinal images using generalized motion pattern. In *2015 Fifth National Conference on Computer Vision, Pattern Recognition, Image Processing and Graphics (NCVPRIPG)*, pages 1–4, 2015.
- [8] L.D. Hubbard, R.J. Brothers, W.N. King, L.X. Clegg, R. Klein, L.S. Cooper, A.R. Sharrett, M.D. Davis, and J. Cai. Methods for evaluation of retinal microvascular abnormalities associated with hypertension/sclerosis in the atherosclerosis risk in communities study. *Ophthalmology*, 106(12):2269–2280, 1999. doi: [http://dx.doi.org/10.1016/S0161-6420\(99\)90525-0](http://dx.doi.org/10.1016/S0161-6420(99)90525-0).
- [9] M. Niemeijer, M.D. Abramoff, and B. van Ginneken. Segmentation of the optic disc, macula and vascular arch in fundus photographs. *IEEE T. Med. Imaging*, 26(1):116–127, 2007.
- [10] J.P. Medhi and S. Dandapat. An effective fovea detection and automatic assessment of diabetic maculopathy in color fundus images. *Comput. Biol. Med.*, 74:30–44, 2016. doi: <http://dx.doi.org/10.1016/j.compbimed.2016.04.007>.
- [11] Q. Cao, J. Liu, and Q. Zhao. Fast automatic optic disc localization in retinal images. In *2013 Seventh International Conference on Image and Graphics*, pages 827–831. IEEE, 2013.
- [12] J. Lowell, A. Hunter, D. Steel, A. Basu, R. Ryder, and E. Fletcher. Optic nerve head segmentation. *IEEE T. Med. Imaging*, 23(2):256–264, 2004.
- [13] E. J. Carmona, M. Rincón, J. García-Feijoo, and J. M. Martínez-de-la Casa. Identification of the optic nerve head with genetic algorithms. *Artif. Intell. Med.*, 43:243–259, 2008.

- [14] A. Aquino, M.E. Gegúndez-Arias, and D. Marin. Detecting the optic disc boundary in digital fundus images using morphological, edge detection, and feature extraction techniques. *IEEE T. Med. Imaging*, 29(11):1860–1869, 2010.
- [15] D. Welfer, J. Scharcanski, C.M. Kitamura, M.M. Dal Pizzol, L.W.B Ludwig, and D. Ruschel. Segmentation of the optic disk in color eye fundus images using an adaptive morphological approach. *Comput. Biol. Med.*, 40:124–137, 2010.
- [16] D. Marin, M.E. Gegundez-Arias, A. Suero, and J.M. Bravo. Obtaining optic disc center and pixel region by automatic thresholding methods on morphologically processed fundus images. *Comput. Meth. Prog. Bio.*, 118(2):173 – 185, 2015. doi: <http://dx.doi.org/10.1016/j.cmpb.2014.11.003>.
- [17] C. Sinthanayothin, J.F. Boyce, H.L. Cook, and T.H. Williamson. Automated localisation of the optic disc, fovea, and retinal blood vessels from digital colour fundus images. *Brit. J. Ophthalmol.*, 83(8):902–910, 1999.
- [18] J. Novo, M.G. Penedo, and J. Santos. Localisation of the optic disc by means of ga-optimised topological active nets. *Image Vision Comput.*, 27(10):1572–1584, 2009.
- [19] L. Xiong and H. Li. An approach to locate optic disc in retinal images with pathological changes. *Computerized Medical Imaging and Graphics*, 47:40–50, 2016.
- [20] O. Chutatape. Fundus foveal localization based on vessel model. In *Engineering in Medicine and Biology Society, 2006. EMBS '06. 28th Annual International Conference of the IEEE*, pages 4440–4444, 2006. doi: [10.1109/IEMBS.2006.260741](http://dx.doi.org/10.1109/IEMBS.2006.260741).
- [21] D. Welfer, J. Scharcanski, and D.R. Marinho. Fovea center detection based on the retina anatomy and mathematical morphology. *Comput. Meth. Prog. Bio.*, 104(3):397–409, 2011. doi: <http://dx.doi.org/10.1016/j.cmpb.2010.07.006>.
- [22] E.F. Kao, P.-C. Lin, M.-C. Chou, T.S. Jaw, and G.C. Liu. Automated detection of fovea in fundus images based on vessel-free zone and adaptive gaussian template. *Comput. Meth. Prog. Bio.*, 117(2):92 – 103, 2014. doi: <http://dx.doi.org/10.1016/j.cmpb.2014.08.003>.
- [23] B. Dashtbozorg, J. Zhang, F. Huang, and B. M. ter Haar Romeny. Automatic optic disc and fovea detection in retinal images using super-elliptical convergence index filters. In A. Campilho and F. Karray, editors, *Image Analysis and Recognition*, pages 697–706. Springer, 2016.
- [24] K. W. Tobin, E. Chaum, V. P. Govindasamy, and T. P. Karnowski. Detection of anatomic structures in human retinal imagery. *IEEE T. Med. Imaging*, 26(12):1729–1739, 2007.

- [25] A.D. Fleming, K.A. Goatman, S. Philip, J.A. Olson, and P.F. Sharp. Automatic detection of retinal anatomy to assist diabetic retinopathy screening. *Phys. Med. Biol.*, 52(2):331–345, 2007.
- [26] M. Niemeijer, M.D. Abràmoff, and B. Van Ginneken. Fast detection of the optic disc and fovea in color fundus photographs. *Med. Image Anal.*, 13(6): 859–870, 2009.
- [27] H. Yu, E.S. Barriga, C. Agurto, S. Echegaray, M. Pattichis, G. Zamora, W. Bauman, and P. Soliz. Fast localization of optic disc and fovea in retinal images for eye disease screening. In *Proc. SPIE, Medical Imaging*, volume 7963, pages 796317–796329, 2011.
- [28] MESSIDOR. Messidor database. <http://messidor.crihan.fr>, 2012. (accessed 16.09.15).
- [29] E. Decenciere, X. Zhang, G. Cazuguel, B. Lay, B. Cochener, C. Trone, P. Gain, R. Ordonez, P. Massin, A. Erginay, B. Charton, and J.C. Klein. Feedback on a publicly distributed database: the messidor database. *Image Anal. Stereol.*, 33(3):231–234, 2014. doi: 10.5566/ias.1155.
- [30] DRIONS-DB. Digital retinal images for optic nerve segmentation database. <http://www.ia.uned.es/personal/ejcarmona/DRIONS-DB.html>, 2013. (accessed 16.09.15).
- [31] ONHSD. Optic nerve head segmentation dataset. <http://reviewdb.lincoln.ac.uk/Image/Datasets/ONHSD.aspx>, 2013. (accessed 16.09.15).
- [32] DIARETDB1. The diabetic retinopathy database. <http://www.it.lut.fi/project/imageret/diaretdb1/>, 2015. (accessed 16.09.15).
- [33] T. Kauppi, V. Kalesnykiene, J.K. Kamarainen, L. Lensu, I. Sorri, A. Ranninen, R. Voutilainen, H. Uusitalo, H. Kälviäinen, and J. Pietilä. The diaretdb1 diabetic retinopathy database and evaluation protocol. In *Proceedings of the 11th Conf. on Medical Image Understanding and Analysis*, pages 61–65, 2007.
- [34] A. Aquino. Establishing the macular grading grid by means of fovea centre detection using anatomical-based and visual-based features. *Comput. Biol. Med.*, 55:61–73, 2014.
- [35] A. Atkinson and C. Mazo. Imaged area of the retina. https://www.optos.com/globalassets/documents/casestudies_imagedareaoftheretina.pdf, 2011. (accessed 16.09.15).
- [36] S. Lee, M.D. Abramoff, and J.M. Reinhardt. Retinal atlas statistics from color fundus images. In *Proc. SPIE 7623, Medical Imaging*, pages 762310–762319, 2010.

- [37] J.J. Staal, M.D. Abramoff, M. Niemeijer, M.A. Viergever, and B. van Ginneken. Ridge based vessel segmentation in color images of the retina. *IEEE T. Med. Imaging*, 23(4):501–509, 2004.
- [38] DRIVE. Drive: Digital retinal images for vessel extraction. <http://www.isi.uu.nl/Research/Databases/DRIVE/>, 2004. (accessed 16.09.15).
- [39] J.A. de la Fuente-Arriaga, E. M. Felipe-Riverón, and E. Garduño Calderón. Application of vascular bundle displacement in the optic disc for glaucoma detection using fundus images. *Comput. Biol. Med.*, 47:27–35, 2014.
- [40] A. Giachetti, L. Ballerini, and E. Trucco. Accurate and reliable segmentation of the optic disc in digital fundus images. *J. Med. Imaging*, 1(2): 024001–024001, 2014.
- [41] F. Girard, C. Kavalec, S. Grenier, H. Ben Tahar, and F. Cheriet. Simultaneous macula detection and optic disc boundary segmentation in retinal fundus images. In *Proc. SPIE, Medical Imaging*, volume 9784, pages 97841F1–97841F9, 2016.
- [42] J.M. Molina and E.J. Carmona. Localization and segmentation of the optic nerve head in eye fundus images using pyramid representation and genetic algorithms. In J.M. Ferrández et al, editor, *Foundations on Natural and Artificial Computation (Part I)*, pages 431–440. Springer, 2011.